

First Near-IR Spectroscopic Survey of Neptune Trojans with JWST: Distinct Surface Compositions of Red vs Ultra-Red Neptune Trojans

LARISSA MARKWARDT ¹, BRYAN J. HOLLER ², HSING WEN LIN (林省文) ¹, DAVID W. GERDES ^{3,1},
FRED C. ADAMS ^{3,1}, RENU MALHOTRA ⁴ AND KEVIN J. NAPIER ^{1,5}

¹*Department of Physics, University of Michigan
450 Church Street*

Ann Arbor, MI 48109-1107, USA

²*Space Telescope Science Institute
3700 San Martin Drive*

Baltimore, MD 21218, USA

³*Department of Astronomy, University of Michigan
1085 South University Avenue*

Ann Arbor, MI 48109-1107, USA

⁴*Department of Planetary Sciences
1629 E University Boulevard*

Tucson, AZ 85721, USA

⁵*Michigan Institute for Data Science, University of Michigan
500 Church Street*

Ann Arbor, MI 48109, USA

ABSTRACT

Neptune’s Trojan asteroids have been observed to have a variety of optical colors, most notably red ($g - r < 0.75$) vs. ultra-red ($g - r > 0.75$), but the underlying cause of these different color classifications is unknown. Near-IR spectroscopy can be used as a probe of the surface composition of these objects, as broad ice bands for a variety of materials are present in the near-IR. Here, we present the first results of a spectroscopic survey of Neptune’s Trojan asteroids using the NIRSpec instrument on JWST. We compare the near-IR spectra of eight Neptune Trojans (NTs) based on different optical color classifications and with model spectra of different ices. We find that most of our targets are consistent with a surface covered in a thin layer of H₂O and CO₂ ices, while the only NT to reliably be classified as ultra-red is covered in ice tholins in addition to CO₂. Ice tholins are a known reddening agent when subjected to irradiation, so these results support the hypothesis that differences in optical color are due to differences in irradiation of the surfaces of these bodies. Since NTs have very similar orbits and therefore generally similar levels of irradiation at the current time, our results suggest that these objects have unique origins or there is ongoing processing of the surfaces of these objects through stochastic disturbances such as impacts.

Keywords: Neptune Trojans (1097) — Infrared Spectroscopy (2285) — Surface Ices (2117)

1. INTRODUCTION

Trojan asteroids, which librate around a planet’s stable Lagrange points (L₄ or L₅), are sometimes referred to as fossils from the early Solar System as they are thought to be remnants of our primordial disk. Specifically, Trojans can have orbits which are stable on order the age of the Solar System due to the strength of the 1:1 resonance with their planet (Lykawka et al. 2011; Malhotra & Jeongahn 2011; Ćuk et al. 2012; Gomes & Nesvorný 2016). Moreover,

this resonance relationship means that Trojans are also tied to the orbital evolution of their planet. This link is particularly important for the giant planets, which may have migrated toward or away from the Sun significantly. If a planet migrates, the Lagrangian regions follow, transforming the original population (Kortenkamp et al. 2004). Thus, current day Trojan properties can also be used to constrain evolutionary models (Nesvorný et al. 2013; Parker 2015; Gomes & Nesvorný 2016; Nesvorný et al. 2018). For example, Trojan asteroids of both Jupiter and Neptune have been observed to exist in thick clouds (i.e. have wide inclination distributions); this observation suggests that these objects did not form *in-situ*, but instead are possibly remnant planetesimals that were captured from heliocentric orbits during the epoch of planetary migration (Sheppard & Trujillo 2006; Pirani et al. 2019). Such migration would have occurred in the first several hundred Myr in the history of the Solar System, so they still are remnants of the very early Solar System. Therefore, the physical characteristics of Trojan populations can provide a window to the early Solar System.

If the Neptune Trojan population (NT) did not form *in-situ*, they are likely planetesimals captured from elsewhere in the primordial disk, with the most likely source population being the nearby Kuiper Belt. If that were the case, Trans-Neptunian Objects (TNOs) and NTs should be similar in size and color. The bimodality of red ($g - r < 0.75$) vs. ultra-red ($g - r > 0.75$) TNOs has been well established (Sheppard 2010; Schwarz et al. 2011; Hainaut et al. 2012; Peixinho et al. 2012; Sheppard 2012; Lacerda et al. 2014; Peixinho et al. 2015; Pike et al. 2017; Wong & Brown 2017; Schwamb et al. 2019). Additionally, the centaur population, dynamically transient small bodies which orbit between Jupiter and Neptune, are thought to be supplied by reservoirs that include the NTs (Horner & Lykawka 2010). These objects are also red/ultra-red in color (Peixinho et al. 2012, 2015). Through 2018, no ultra-red NTs had been found, making their color distribution distinctly different than their expected origins or offshoots (Jewitt 2018). Since then, six ultra-red NTs (2011 SO₂₇₇, 2011 HM₁₀₂, 2013 TZ₁₈₇, 2013 VX₃₀, 2014 RO₇₄, 2015 VV₁₆₅) have been identified (Lin et al. 2019; Bolin et al. 2023; Markwardt et al. 2023), and the current red to ultra-red ratio is now in line with the TNO population (Markwardt et al. 2023). Additionally, Markwardt et al. (2023) identified three NTs which appear to be “blue” (i.e. nearly solar) in color; a similarly blue TNO has been observed whose origin is suggested to be the outer asteroid belt (Seccul et al. 2018). The blue NTs may have a similar origin, but their orbits are stable for >Gyrs, so if they are captured objects, they were captured just after Neptune’s migration (Markwardt et al. 2023). Thus, NTs may have originated from across the Solar System, not just the Kuiper Belt.

While it is clear that colors of NTs are tied to the Solar System’s formation and evolution, they are a limited tool for understanding the history and composition of the surfaces of these objects. The limitation is in part due to interplay between independent processes that can all transform the surface of the icy/rocky bodies, including radiation from the solar wind, galactic cosmic rays, charged particles in magnetospheres, ice lines, heating resurfacing events, and impacts (Bennett et al. 2013). In general, we expect that these bodies were originally blue/neutral due to the ices covering their surfaces, then these surfaces become red in color over time due to irradiation. However, impacts can “re-blue” the surface by bringing fresh icy material beneath the irradiation crust back to the surface (Luu & Jewitt 1996). This model can explain the diversity in observed colors, but there are complications, such as the fact that cosmic rays could penetrate to a deep layer on TNOs requiring collisions to be larger to re-blue the surface (Gil-Hutton 2002). Moreover, even though ices should normally be colorless, even a relatively small amount of carbonaceous materials mixed with these ices can darken/redden these surfaces (Cruikshank et al. 2019). In short, a variety of processes and compositions can affect the surfaces of planetary bodies, and colors alone are often not sufficient to disentangle the degeneracies between them.

Fortunately, we can get more information to distinguish these scenarios through near-IR spectroscopy. Near-IR bands (3-5 microns) are especially useful for observing planetary surfaces as many broad molecular absorption features occur at these wavelengths. While some compositions may have similar optical/VNIR spectra, they are easily distinguishable with measurements at wavelengths > 3 microns, meaning that it is possible to measure and distinguish volatile species and complex organics on the surfaces of small bodies through reflectance spectroscopy (Parker et al. 2016). Water ice also has multiple distinct absorption bands in the near-IR, the depth and location of which can be used to measure further surface properties such as grain size and ice phase (Clark & Lucey 1984; Cruikshank et al. 2019). Additionally, ice irradiation products have absorption features in the near-IR that have already been identified on the surfaces of other small bodies through ground-based observations (Brown et al. 2015).

Previous spectroscopic study of the surfaces of TNOs has been limited to the brightest objects that can be observed with ground-based observations (Dalle Ore et al. 2009; Delsanti et al. 2010; Clark et al. 2012; Brown et al. 2015; Seccul et al. 2021; Merlin et al. 2017, & references therein). With V-band magnitudes <21.5 (see Table 1), NTs are well beyond the capabilities of most ground-based observatories. The only observatory currently powerful enough to target

Table 1. Neptune Trojan Spectroscopic Survey Targets

Name	L4/L5	Stability	Average V-band Mag.	Color Classification	Total Obs. Time
2006 RJ ₁₀₃	L4	stable	22.5	red ^{abf}	2.0 hrs
2007 VL ₃₀₅	L4	stable	22.8	red ^{abf}	2.4 hrs
2008 LC ₁₈	L5	meta-stable	23.5	red ^e	4.8 hrs
2010 TS ₁₉₁	L4	meta-stable	22.9	red ^{cf}	2.9 hrs
2011 HM ₁₀₂	L5	stable	23.1	red ^b /ultra-red ^e	3.4 hrs
2011 SO ₂₇₇	L4	stable	22.6	red ^d /ultra-red ^f	2.4 hrs
2011 WG ₁₅₇	L4	stable	22.3	red ^d	2.0 hrs
2013 VX ₃₀	L4	stable	22.8	ultra-red ^{def}	2.2 hrs

NOTE—Stability taken from [Lin et al. \(2021\)](#). Ave V-band magnitude calculated by [Horizons](#) using [astroquery.jplhorizons](#).

Color classifications are taken from the literature – ^a [Sheppard \(2012\)](#) ^b [Parker et al. \(2013\)](#) ^c [Jewitt \(2018\)](#) ^d [Lin et al. \(2019\)](#) ^e [Bolin et al. \(2023\)](#) ^f [Markwardt et al. \(2023\)](#)

NTs is the recently launched JWST. In this paper we present the initial results of the first near-IR spectra of a subset of the NT population, observed with JWST.

The structure of this paper is as follows: Section 2 describes the design of our spectroscopic survey. Section 3 outlines our data reduction and spectral modeling process. Section 4 presents the results of our survey. Section 5 discusses the conclusions drawn from our results.

2. SURVEY DESIGN

The goal of this project is to measure the near-IR spectra of several NTs to identify surface ice features and compare them based on L4 vs L5, red vs ultra-red, and stability. Our target list is shown in Table 1, and includes 2013 VX₃₀, the first ultra-red NT discovered. Specific targets were chosen based on total exposure time constraints for this program while still representing all of the described populations.

We chose to use the NIRSpec IFU instrument on JWST to conduct our spectroscopic survey, due to its wavelength coverage, field of view (FOV), and low resolution capabilities. As stated previously (see Sec. 1), the wavelength coverage of NIRSpec (0.5 - 5 microns) is ideal for measuring near-IR absorption bands of common materials on the surfaces of outer Solar System objects. We chose to use the IFU for these observations rather than one of the fixed slits due to its larger field of view. With the 3σ pointing uncertainty of JWST (0.3") and the positional uncertainty of our objects, it would have been very difficult to accurately place the target within the slits. Therefore, we instead opted for blind pointing in the IFU aperture, which requires the uncertainty only be less than 1.5". We conducted a photometric survey using the Magellan 6.5m Baade Telescope located at Las Campanas Observatory and the Hiltner 2.4m Telescope located at the Kitt Peak National Observatory to constrain the orbits of our targets to an uncertainty within the FOV ([Markwardt et al. 2023](#)). Finally, our observations are of broad absorption features so we did not require high resolution to meet our goals; therefore, we utilized the PRISM mode on the instrument to maximize SNR. We used the *NRSIRS2RAPID* readout mode to improve performance and sensitivity in long exposure IFU observations of our faint targets. We opted for a large (0.5") 4 point dither for our background extraction. The 4 point dither pattern was chosen instead of a 2 point nod for additional redundancy against detector defects and MSA light leakage that can contaminate the IFU spectrum, as well as to provide improved spatial sampling. We were able to use the large pattern by re-observing our targets to derive smaller positional uncertainties.

3. DATA ANALYSIS

3.1. Data Reduction

Our analysis uses the 3D data cubes created with the JWST calibration pipeline version 1.11.4 and the `jwst.1122.pmap` reference file context. Extraction of the target spectrum from the 3D data cube is best handled via aperture photometry within each wavelength slice (i.e., within each image of the data cube). However, aperture photometry directly on the data increases the noise in the resulting spectrum; the better option is to perform aperture

photometry on a scaled point-spread function (PSF) model fit to the data in order to remove artifacts and cosmic rays. For each wavelength slice, we constructed empirical PSF models (referred to as “template PSFs”; Ian Wong, personal communication) using a moving median on the 10 slices shortward and longward of the considered slice (21 slices total). For slices close to the short- or long-wavelength end of the cube, less than 21 total slices were used to create the template, resulting in slightly higher noise in these regions. Use of a small wavelength window reduces variations in the background and the PSF. The background was subtracted from each slice individually prior to the calculation of the median, then the template PSF was trimmed to a 9×9 pixel box (all other pixels set to NaN) and normalized to unity within the box. The template was then used as the model for a fit with two parameters: a flux scaling factor and a background. The best-fit parameters were determined by using the `scipy.optimize.minimize` Python routine to minimize the χ^2 of the residual (data minus model) using a Nelder-Mead downhill simplex algorithm (also known as the amoeba fitting routine; Press et al. 2007). After determining the best-fit parameters, the template was multiplied by the flux scaling factor, the centroid was computed in the image, and a 3.5-pixel radius circular extraction aperture centered on the centroid was used to extract the flux. This process was performed at each wavelength to extract the full 1D spectrum from 0.7 - 5.1 μm (the noisier portions of the spectrum $<0.7 \mu\text{m}$ and $>5.1 \mu\text{m}$ were trimmed prior to carrying out the extraction process). The same process was also carried out for a G-type standard star (SNAP-2 from PID 1128). The 1D spectra from all dithers of a given observation were resampled onto the wavelength grid of the standard star, median-combined, and divided by the standard star to remove the solar component. Finally, outliers were identified and removed using a 21-point moving median and a $2.5\text{-}\sigma$ threshold; any points above the threshold were replaced with the value of the moving median. The resulting spectra, organized by measured spectral slope at $<1 \mu\text{m}$, are shown in Fig. 1.

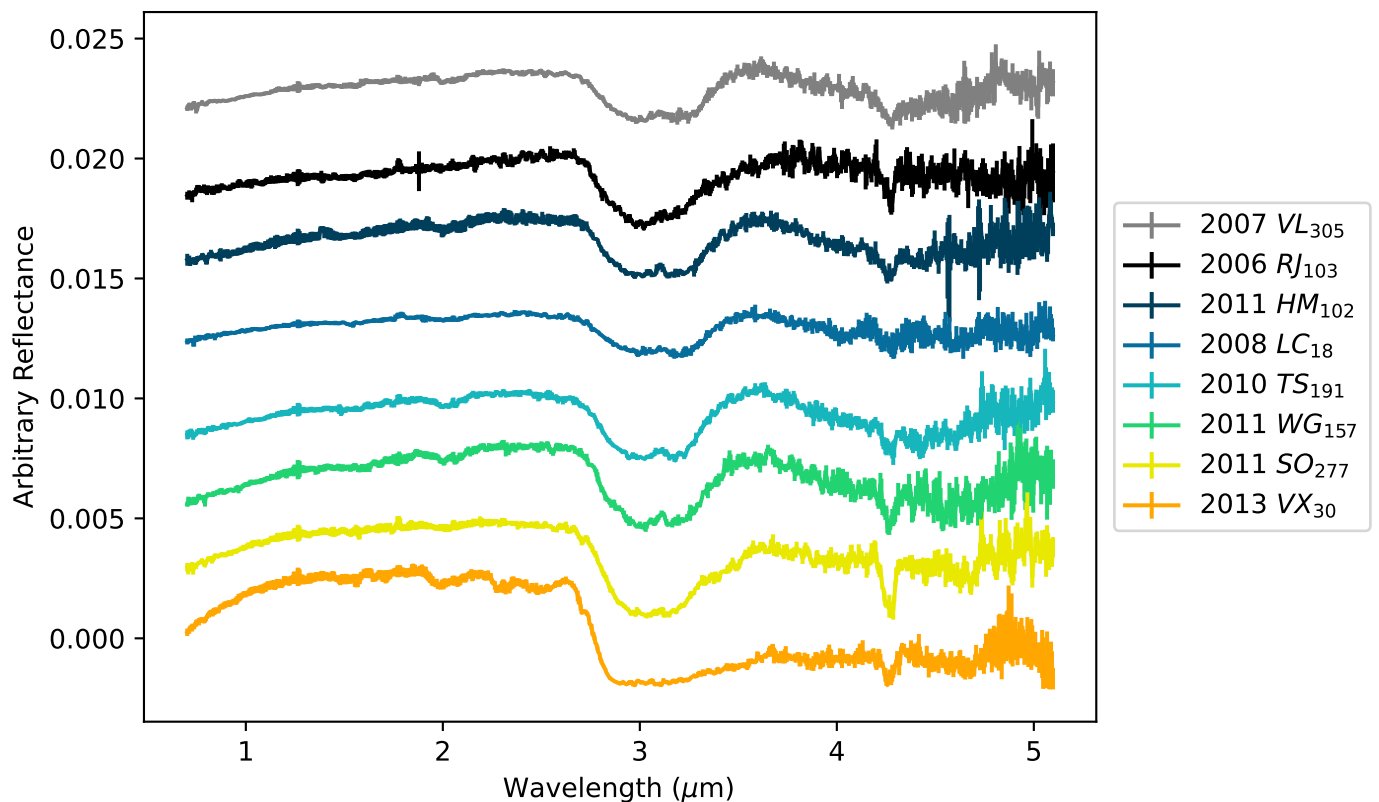


Figure 1. NIRSPEC 1D spectra plotted with their observational errors for all of the NT targets. Each spectrum has been shifted vertically by an arbitrary amount such that the spectra are organized from smallest to largest spectral slope at $<1 \mu\text{m}$. All of the spectra have exhibit a CO_2 absorption feature at $4.25 \mu\text{m}$ and a strong $3.1 \mu\text{m}$ Fresnel peak associated with water ice, with the exception of 2013 *VX*₃₀, which has a much broader feature at that wavelength range (see also Sec. 4 and Fig. 2). Thus, the most red NT in our sample has a near-IR spectrum which is clearly distinct from the others included in our observations.

Table 2. Ice Optical Constant Experimental Parameters

Material	Phase	Temperature (K)	Pressure (mbar)	Experiment Reference
H ₂ O	Amorphous	50	1e - 8	Mastrapa et al. (2009)
H ₂ O	Crystalline	50	1e - 8	Mastrapa et al. (2009)
CO ₂	Crystalline	179	Not available	Quirico & Schmitt (2004), Schmitt et al. (2018)
Titan Tholin		Not available	0.26	Imanaka et al. (2012)
Triton Tholin		290	0.2	Khare et al. (1984)

3.2. Spectral Modeling

We fit the observed 1D spectra of our targets by implementing a spectral model composed of ices expected or known to exist on the surfaces of small bodies in the outer Solar System (Fernández-Valenzuela et al. 2021). Based on visual inspection of the features observed in our dataset, we specifically included H₂O, CO₂, and tholins in our model. We implemented a Mie scattering (Mie 1908) model using the `miepython` Python module (Prah 2023). This model uses optical constants of a medium to calculate the extinction efficiency, scattering efficiency, backscattering, and scattering asymmetry. The extinction and scattering efficiencies can then be used to calculate the absorption cross-section by:

$$\sigma = (Q_{ext} - Q_{sca})\pi r^2 \quad (1)$$

where σ is the absorption cross-sectional area, Q_{ext} is the extinction efficiency, Q_{sca} is the scattering efficiency, and r is the particle radius. A simplistic model, which reproduced our data, is a thin layer of material over a reflective surface, similar to the model in Brown & Fraser (2023). Specifically, we utilize the absorption cross-section and the Beer-Lambert Law to calculate the reflectance at each wavelength:

$$\frac{I}{I_0} = e^{-\sigma N} \quad (2)$$

where $\frac{I}{I_0}$ is the reflectance and N is the column density of the material. The optical constants for the materials used in our models were obtained from published experimental measurements; the physical parameters of these experiments (phase, temperature, pressure) are listed in Table 2.

4. RESULTS

The resulting spectra and model fits are shown in Fig. 2, and the best fit model parameters are included in Table 3. Overall, most of these spectra look relatively similar, each displaying a strong 3.1 μm Fresnel peak associated with water ice and a CO₂ absorption feature at 4.25 μm . These spectra also look remarkably similar to that of Saturn’s moon, Iapetus, particularly including a double-peaked feature at 3.1 μm , a broad water ice feature from 3.5 - 5 μm , and a narrow CO₂ absorption feature at 4.25 μm ; Iapetus has also been identified to be covered with water and CO₂ ice (Clark et al. 2012). CO₂ has also been observed on the surfaces of Kuiper Belt Objects using JWST (Brown & Fraser 2023). This result demonstrates a consistency in surface composition across the outer Solar System.

However, there is a clear difference in the spectrum of 2013 VX₃₀ which does exhibit the 4.25 μm CO₂ feature but with a much deeper and broader feature near 3 μm ; this spectrum has a much better fit to an ice tholin dominated model (specifically the Triton tholin model). This is the only NT in this dataset that has been consistently observed to be ultra-red in color (see Table 1). Ice tholins are a known reddening agent and are likely the explanation for why this object has an ultra-red optical color (Cruikshank et al. 2005). The other ultra-red NTs, 2011 HM₁₀₂ and 2011 SO₂₇₇, do not exhibit this ice tholin feature on the other hand. The fact that these objects have variable color classifications may point to inhomogeneities in the surface composition of these objects that are not captured in these observations. However, even if 2011 SO₂₇₇ does have a surface ice composition dominated by water ice, this target is more consistent with the amorphous water ice model which could also be due to UV irradiation (Kouchi & Kuroda 1990; Moore & Hudson 1992).

5. DISCUSSION

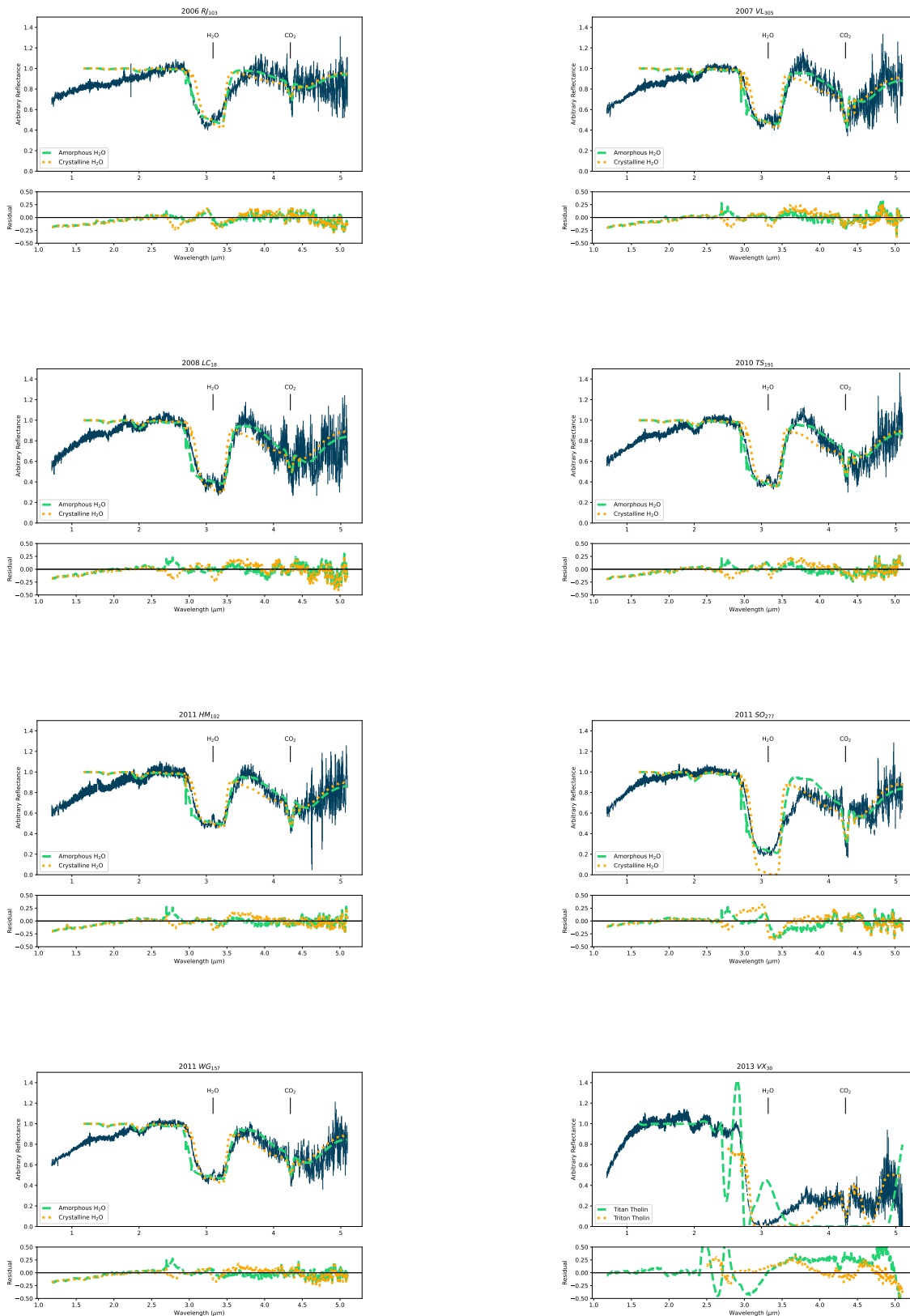


Figure 2. NIRSpectra and surface ice compositional models. The NIRSpectra data with observational errors is shown as a navy line in each of the upper panels. Each spectrum has been arbitrarily rescaled based on the mean value between ~ 2 and 3 microns. The spectral fits are shown as a green dashed or orange dotted line in the upper panels and the corresponding residuals of the fit are shown in the lower panels; the green dashed line corresponds to a model with amorphous H₂O and the orange dotted line corresponds to a model with crystalline H₂O, except in the case of 2013VX₃₀ where these lines correspond to models with Titan tholins and Triton tholins respectively.

Table 3. Surface Ice Composition Modeling Results

Model Name	Ice	Radius (μm)	Column Density (μm^{-2})
2006 RJ ₁₀₃ Model 1	Amorphous H ₂ O	$2.7105 \pm 1.36 \times 10^{-3}$	$2.4014 \times 10^{-2} \pm 2.80 \times 10^{-5}$
	CO ₂	$8.2756 \times 10^{-1} \pm 2.85 \times 10^{-3}$	$4.5347 \times 10^{-2} \pm 3.81 \times 10^{-4}$
2006 RJ ₁₀₃ Model 2	Crystalline H ₂ O	$1.6580 \pm 1.04 \times 10^{-3}$	$6.6922 \times 10^{-2} \pm 9.90 \times 10^{-5}$
	CO ₂	$8.1432 \times 10^{-1} \pm 4.34 \times 10^{-3}$	$3.5112 \times 10^{-2} \pm 4.60 \times 10^{-4}$
2007 VL ₃₀₅ Model 1	Amorphous H ₂ O	$4.8044 \pm 1.12 \times 10^{-3}$	$8.8019 \times 10^{-3} \pm 5.11 \times 10^{-6}$
	CO ₂	$9.9324 \times 10^{-1} \pm 2.22 \times 10^{-3}$	$7.1998 \times 10^{-2} \pm 3.45 \times 10^{-4}$
2007 VL ₃₀₅ Model 2	Crystalline H ₂ O	$2.7564 \pm 7.03 \times 10^{-4}$	$2.7385 \times 10^{-2} \pm 1.86 \times 10^{-5}$
	CO ₂	$1.4749 \pm 3.41 \times 10^{-3}$	$2.5463 \times 10^{-2} \pm 1.16 \times 10^{-4}$
2008 LC ₁₈ Model 1	Amorphous H ₂ O	$5.1893 \pm 8.40 \times 10^{-4}$	$9.4951 \times 10^{-3} \pm 4.25 \times 10^{-6}$
	CO ₂	$1.3843 \pm 3.25 \times 10^{-3}$	$1.8349 \times 10^{-2} \pm 9.37 \times 10^{-5}$
2008 LC ₁₈ Model 2	Crystalline H ₂ O	$2.4627 \pm 7.92 \times 10^{-4}$	$4.7721 \times 10^{-2} \pm 4.08 \times 10^{-5}$
	CO ₂	$9.2363 \times 10^{-1} \pm 4.73 \times 10^{-3}$	$3.4879 \times 10^{-2} \pm 3.85 \times 10^{-4}$
2010 TS ₁₉₁ Model 1	Amorphous H ₂ O	$4.1032 \pm 9.44 \times 10^{-4}$	$1.5425 \times 10^{-2} \pm 9.10 \times 10^{-6}$
	CO ₂	$9.6849 \times 10^{-1} \pm 2.32 \times 10^{-3}$	$6.6659 \times 10^{-2} \pm 3.40 \times 10^{-4}$
2010 TS ₁₉₁ Model 2	Crystalline H ₂ O	$2.7595 \pm 6.09 \times 10^{-4}$	$3.3486 \times 10^{-2} \pm 2.02 \times 10^{-5}$
	CO ₂	$9.2821 \times 10^{-1} \pm 3.35 \times 10^{-3}$	$4.7194 \times 10^{-2} \pm 3.68 \times 10^{-4}$
2011 HM ₁₀₂ Model 1	Amorphous H ₂ O	$5.8172 \pm 8.54 \times 10^{-4}$	$5.7245 \times 10^{-3} \pm 2.34 \times 10^{-6}$
	CO ₂	$9.8437 \times 10^{-1} \pm 2.36 \times 10^{-3}$	$6.1510 \times 10^{-2} \pm 3.14 \times 10^{-4}$
2011 HM ₁₀₂ Model 2	Crystalline H ₂ O	$3.3738 \pm 5.73 \times 10^{-4}$	$1.7505 \times 10^{-2} \pm 8.41 \times 10^{-6}$
	CO ₂	$9.5797 \times 10^{-1} \pm 3.06 \times 10^{-3}$	$4.9331 \times 10^{-2} \pm 3.35 \times 10^{-4}$
2011 SO ₂₇₇ Model 1	Amorphous H ₂ O	$3.6019 \pm 1.14 \times 10^{-3}$	$2.9292 \times 10^{-2} \pm 2.37 \times 10^{-5}$
	CO ₂	$8.7823 \times 10^{-1} \pm 1.65 \times 10^{-3}$	$9.9733 \times 10^{-2} \pm 4.41 \times 10^{-4}$
2011 SO ₂₇₇ Model 2	Crystalline H ₂ O	$9.7455 \times 10^{-1} \pm 7.34 \times 10^{-4}$	$1.1031 \pm 2.75 \times 10^{-3}$
	CO ₂	$8.4777 \times 10^{-1} \pm 2.42 \times 10^{-3}$	$7.2045 \times 10^{-2} \pm 4.94 \times 10^{-4}$
2011 WG ₁₅₇ Model 1	Amorphous H ₂ O	$6.1873 \pm 7.26 \times 10^{-4}$	$5.5075 \times 10^{-3} \pm 1.97 \times 10^{-6}$
	CO ₂	$9.2405 \times 10^{-1} \pm 2.69 \times 10^{-3}$	$4.6976 \times 10^{-2} \pm 2.98 \times 10^{-4}$
2011 WG ₁₅₇ Model 2	Crystalline H ₂ O	$3.4350 \pm 4.74 \times 10^{-4}$	$1.8777 \times 10^{-2} \pm 7.66 \times 10^{-6}$
	CO ₂	$8.7865 \times 10^{-1} \pm 3.24 \times 10^{-3}$	$3.6643 \times 10^{-2} \pm 3.07 \times 10^{-4}$
2013 VX ₃₀ Model 1	Titan Tholin	$3.2782 \times 10^1 \pm 1.77 \times 10^{-1}$	$1.7017 \times 10^1 \pm 1.82 \times 10^{-1}$
	CO ₂	$1.0249 \times 10^{-2} \pm 4.83 \times 10^4$	$5.1629 \times 10^{-5} \pm 7.43 \times 10^2$
2013 VX ₃₀ Model 2	Triton Tholin	$1.5055 \pm 4.17 \times 10^{-4}$	$2.4229 \pm 2.24 \times 10^{-3}$
	CO ₂	$9.8666 \times 10^{-1} \pm 3.89 \times 10^{-3}$	$6.9471 \times 10^{-2} \pm 5.82 \times 10^{-4}$

The main result of this paper is that red and ultra-red surfaces have distinguishable compositions. In particular, while red NTs are covered in H₂O and CO₂ ice, ultra-red NTs are covered in ice tholins. Ice tholins are a complex organic, black tar-like substance that is formed when cosmogonically abundant molecules or ices, such as CO₂ and H₂O ice, are irradiated by the Sun (Sagan & Khare 1979; Khare et al. 1989). There are several explanations as to why we observe two compositionally distinct groups of NTs.

- One possible explanation is that these two compositional groups come from two distinct source populations. Each group could have its distinct starting composition and chemical evolution due to forming at distinctly different locations in the Solar System. These two populations could have been subsequently mixed during planetary migration. In this way, the differences between the two populations would be primordial. If there is a sharp distinction between the two populations this may also explain the bimodality in spectra observed.
- Since irradiation of H₂O and CO₂ can create tholins, red objects may turn into ultra-red over time given enough exposure to the Sun. In this case the differences between populations would be due to differences in irradiation. However, with NTs all having the same orbital distance with the same level of solar exposure, it is not clear why

some would be more irradiated than others, unless these objects were irradiated differently prior to their capture in the Trojan cloud.

- Finally, if these objects are from the same source and experience the same levels of irradiation, their differences could be due to meteoroidal impacts on the surface. [Luu & Jewitt \(1996\)](#) have shown that tholins may only form a thin layer on the surface, and impacts can bring the underlying ice back to the surface. In this way, we can explain the similarity in composition, both have CO₂ ice, and the differences, each object is at a varying stage of irradiation or impacts. This explanation may account for why a high-inclination NT is ultra-red as it would be more likely to avoid impacts that would re-blue the surface. In this scenario one would expect a smooth transition between optical color where each object is at a unique state within a continuum of states, as has been observed in [Markwardt et al. \(2023\)](#).

In order to distinguish between these different scenarios, further observations and analysis are needed. Completing the observations for the rest of our target list will allow us to compare spectroscopic results based on the orbital stability of our targets, which will give us clues as to whether primordial NTs are at all distinct from those captured more recently, which would have unique origins. Additionally, a more geometrically realistic model of the reflectance of the surface of these objects (such as using Hapke modeling; [Hapke 1993](#)), would also allow us to constrain the thickness of these thin ice layers of the surface. A more in-depth model for this dataset is planned for the future once all of the targets have been observed. Results from [Brown & Fraser \(2023\)](#) seem to indicate that these layers are only a few microns thick, suggesting that they are relatively delicate and potential short-lived features. Observing how the surfaces of these objects change over time, potentially through lightcurve variations, may give us a better picture into the dynamics of the surfaces of these objects. Moreover, discovering and studying the smallest members of the NT population will be key to testing theories of outward volatile transport ([Brown & Fraser 2023](#)) and lead us to better constraints on the collisional history of this population, which may be the key to produce spectrally distinct members within the same population.

However, it is currently clear that, for whatever reason, there are spectrally distinct NTs, and their spectra correlate with their optical color. Whether these objects are also spectrally similar to their presumed population of origin, the Kuiper Belt, is beyond the scope of this paper. A similar JWST program studying the surface composition of a large sample of TNOs is also ongoing (PID 2418, PI Pinilla-Alonso); comparisons between these populations will be the key to tying their origins together, something only hinted at by their colors. Unfortunately, no observations of the newly identified blue NTs ([Markwardt et al. 2023](#)) are currently planned. Such a future study may be valuable to determining whether these objects have more in common with objects elsewhere in the Solar System based on their composition. Addressing these questions will be key to our understanding of the chemical and dynamical history of the outer Solar System, giving us a key window into the primordial material that makes the building blocks of our planets.

We thank Mike Brown and Charles Proffitt for helpful conversations that greatly improved this paper.

All of the data presented in this paper were obtained from the Mikulski Archive for Space Telescopes (MAST) at the Space Telescope Science Institute. The specific observations analyzed can be accessed via <https://doi.org/10.17909/j66s-pv96>. STScI is operated by the Association of Universities for Research in Astronomy, Inc., under NASA contract NAS5-26555. Support to MAST for these data is provided by the NASA Office of Space Science via grant NAG5-7584 and by other grants and contracts.

Support for program #2550 was provided by NASA through a grant from the Space Telescope Science Institute, which is operated by the Association of Universities for Research in Astronomy, Inc., under NASA contract NAS 5-03127.

Facilities: JWST (NIRSpec)

REFERENCES

- Bennett, C. J., Pirim, C., & Orlando, T. M. 2013, *Chemical Reviews*, 113, 9086, doi: [10.1021/cr400153k](https://doi.org/10.1021/cr400153k)
- Bolin, B. T., Fremling, C., Morbidelli, A., et al. 2023, *MNRAS*, 521, L29, doi: [10.1093/mnrasl/slad018](https://doi.org/10.1093/mnrasl/slad018)

- Brown, M. E., & Fraser, W. C. 2023, PSJ, 4, 130, doi: [10.3847/PSJ/ace2ba](https://doi.org/10.3847/PSJ/ace2ba)
- Brown, M. E., Schaller, E. L., & Blake, G. A. 2015, AJ, 149, 105, doi: [10.1088/0004-6256/149/3/105](https://doi.org/10.1088/0004-6256/149/3/105)
- Clark, R. N., & Lucey, P. G. 1984, J. Geophys. Res., 89, 6341, doi: [10.1029/JB089iB07p06341](https://doi.org/10.1029/JB089iB07p06341)
- Clark, R. N., Cruikshank, D. P., Jaumann, R., et al. 2012, Icarus, 218, 831, doi: <https://doi.org/10.1016/j.icarus.2012.01.008>
- Cruikshank, D. P., Imanaka, H., & Dalle Ore, C. M. 2005, Advances in Space Research, 36, 178, doi: [10.1016/j.asr.2005.07.026](https://doi.org/10.1016/j.asr.2005.07.026)
- Cruikshank, D. P., Moroz, L. V., & Clark, R. N. 2019, Spectroscopy of Ices, Volatiles, and Organics in the Visible and Infrared Regions, ed. J. L. Bishop, I. Bell, James F., & J. E. Moersch, 102–119, doi: [10.1017/9781316888872.007](https://doi.org/10.1017/9781316888872.007)
- Ćuk, M., Hamilton, D. P., & Holman, M. J. 2012, MNRAS, 426, 3051, doi: [10.1111/j.1365-2966.2012.21964.x](https://doi.org/10.1111/j.1365-2966.2012.21964.x)
- Dalle Ore, C. M., Barucci, M. A., Emery, J. P., et al. 2009, A&A, 501, 349, doi: [10.1051/0004-6361/200911752](https://doi.org/10.1051/0004-6361/200911752)
- Delsanti, A., Merlin, F., Guilbert-Lepoutre, A., et al. 2010, A&A, 520, A40, doi: [10.1051/0004-6361/201014296](https://doi.org/10.1051/0004-6361/201014296)
- Fernández-Valenzuela, E., Pinilla-Alonso, N., Stansberry, J., et al. 2021, PSJ, 2, 10, doi: [10.3847/PSJ/abc34e](https://doi.org/10.3847/PSJ/abc34e)
- Gil-Hutton, R. 2002, Planet. Space Sci., 50, 57, doi: [10.1016/S0032-0633\(01\)00073-3](https://doi.org/10.1016/S0032-0633(01)00073-3)
- Gomes, R., & Nesvorný, D. 2016, A&A, 592, A146, doi: [10.1051/0004-6361/201527757](https://doi.org/10.1051/0004-6361/201527757)
- Hainaut, O. R., Boehnhardt, H., & Protopapa, S. 2012, A&A, 546, A115, doi: [10.1051/0004-6361/201219566](https://doi.org/10.1051/0004-6361/201219566)
- Hapke, B. 1993, Theory of reflectance and emittance spectroscopy
- Horner, J., & Lykawka, P. S. 2010, MNRAS, 402, 13, doi: [10.1111/j.1365-2966.2009.15702.x](https://doi.org/10.1111/j.1365-2966.2009.15702.x)
- Imanaka, H., Cruikshank, D. P., Khare, B. N., & McKay, C. P. 2012, Icarus, 218, 247, doi: [10.1016/j.icarus.2011.11.018](https://doi.org/10.1016/j.icarus.2011.11.018)
- Jewitt, D. 2018, AJ, 155, 56, doi: [10.3847/1538-3881/aaa1a4](https://doi.org/10.3847/1538-3881/aaa1a4)
- Khare, B. N., Sagan, C., Arakawa, E. T., et al. 1984, Icarus, 60, 127, doi: [10.1016/0019-1035\(84\)90142-8](https://doi.org/10.1016/0019-1035(84)90142-8)
- Khare, B. N., Thompson, W. R., Chyba, C. F., Arakawa, E. T., & Sagan, C. 1989, Advances in Space Research, 9, 41, doi: [10.1016/0273-1177\(89\)90362-1](https://doi.org/10.1016/0273-1177(89)90362-1)
- Kortenkamp, S. J., Malhotra, R., & Michtchenko, T. 2004, Icarus, 167, 347, doi: [10.1016/j.icarus.2003.09.021](https://doi.org/10.1016/j.icarus.2003.09.021)
- Kouchi, A., & Kuroda, T. 1990, Nature, 344, 134, doi: [10.1038/344134a0](https://doi.org/10.1038/344134a0)
- Lacerda, P., Fornasier, S., Lellouch, E., et al. 2014, ApJL, 793, L2, doi: [10.1088/2041-8205/793/1/L2](https://doi.org/10.1088/2041-8205/793/1/L2)
- Lin, H. W., Gerdes, D. W., Hamilton, S. J., et al. 2019, Icarus, 321, 426, doi: [10.1016/j.icarus.2018.12.006](https://doi.org/10.1016/j.icarus.2018.12.006)
- Lin, H. W., Chen, Y.-T., Volk, K., et al. 2021, Icarus, 361, 114391, doi: [10.1016/j.icarus.2021.114391](https://doi.org/10.1016/j.icarus.2021.114391)
- Luu, J., & Jewitt, D. 1996, AJ, 112, 2310, doi: [10.1086/118184](https://doi.org/10.1086/118184)
- Lykawka, P. S., Horner, J., Jones, B. W., & Mukai, T. 2011, MNRAS, 412, 537, doi: [10.1111/j.1365-2966.2010.17936.x](https://doi.org/10.1111/j.1365-2966.2010.17936.x)
- Malhotra, R., & Jeongahn, Y. 2011, in EPSC-DPS Joint Meeting 2011, Vol. 2011, 1215
- Markwardt, L., Wen Lin, H., Gerdes, D., & Adams, F. C. 2023, PSJ, 4, 135, doi: [10.3847/PSJ/ace528](https://doi.org/10.3847/PSJ/ace528)
- Mastrapa, R. M., Sandford, S. A., Roush, T. L., Cruikshank, D. P., & Dalle Ore, C. M. 2009, ApJ, 701, 1347, doi: [10.1088/0004-637X/701/2/1347](https://doi.org/10.1088/0004-637X/701/2/1347)
- Merlin, F., Hromakina, T., Perna, D., Hong, M. J., & Alvarez-Candal, A. 2017, A&A, 604, A86, doi: [10.1051/0004-6361/201730933](https://doi.org/10.1051/0004-6361/201730933)
- Mie, G. 1908, Annalen der Physik, 330, 377, doi: [10.1002/andp.19083300302](https://doi.org/10.1002/andp.19083300302)
- Moore, M. H., & Hudson, R. L. 1992, ApJ, 401, 353, doi: [10.1086/172065](https://doi.org/10.1086/172065)
- Nesvorný, D., Vokrouhlický, D., Bottke, W. F., & Levison, H. F. 2018, Nature Astronomy, 2, 878, doi: [10.1038/s41550-018-0564-3](https://doi.org/10.1038/s41550-018-0564-3)
- Nesvorný, D., Vokrouhlický, D., & Morbidelli, A. 2013, ApJ, 768, 45, doi: [10.1088/0004-637X/768/1/45](https://doi.org/10.1088/0004-637X/768/1/45)
- Parker, A., Pinilla-Alonso, N., Santos-Sanz, P., et al. 2016, Publ. Astron. Soc. Pacific, 128, 18010, doi: [10.1088/1538-3873/128/959/018010](https://doi.org/10.1088/1538-3873/128/959/018010)
- Parker, A. H. 2015, Icarus, 247, 112, doi: [10.1016/j.icarus.2014.09.043](https://doi.org/10.1016/j.icarus.2014.09.043)
- Parker, A. H., Buie, M. W., Osip, D. J., et al. 2013, AJ, 145, 96, doi: [10.1088/0004-6256/145/4/96](https://doi.org/10.1088/0004-6256/145/4/96)
- Peixinho, N., Delsanti, A., & Doressoundiram, A. 2015, A&A, 577, A35, doi: [10.1051/0004-6361/201425436](https://doi.org/10.1051/0004-6361/201425436)
- Peixinho, N., Delsanti, A., Guilbert-Lepoutre, A., Gafeira, R., & Lacerda, P. 2012, A&A, 546, A86, doi: [10.1051/0004-6361/201219057](https://doi.org/10.1051/0004-6361/201219057)
- Pike, R. E., Fraser, W. C., Schwamb, M. E., et al. 2017, AJ, 154, 101, doi: [10.3847/1538-3881/aa83b1](https://doi.org/10.3847/1538-3881/aa83b1)
- Pirani, S., Johansen, A., & Mustill, A. J. 2019, A&A, 631, A89, doi: [10.1051/0004-6361/201936600](https://doi.org/10.1051/0004-6361/201936600)
- Prahl, S. 2023, miepython: Pure python implementation of Mie scattering, v2.5.3, Zenodo, doi: [10.5281/zenodo.8218010](https://doi.org/10.5281/zenodo.8218010)
- Press, D., Götzinger, S., Reitzenstein, S., et al. 2007, PhRvL, 98, 117402, doi: [10.1103/PhysRevLett.98.117402](https://doi.org/10.1103/PhysRevLett.98.117402)

- Quirico, E., & Schmitt, B. 2004, “Near-IR optical constants of crystalline CO₂ ice at 179 K completed with 28K data”, Dataset/Spectral Data, SSHADE/GhoSST (OSUG Data Center), doi: https://doi.org/10.26302/SSHADE/EXPERIMENT_BS_20130215_001
- Sagan, C., & Khare, B. N. 1979, *Nature*, 277, 102, doi: [10.1038/277102a0](https://doi.org/10.1038/277102a0)
- Schmitt, B., Bollard, P., Albert, D., et al. 2018, SSHADE: “Solid Spectroscopy Hosting Architecture of Databases and Expertise” and its databases, Service/Database Infrastructure, OSUG Data Center, doi: [10.26302/SSHADE](https://doi.org/10.26302/SSHADE)
- Schwamb, M. E., Fraser, W. C., Bannister, M. T., et al. 2019, *ApJS*, 243, 12, doi: [10.3847/1538-4365/ab2194](https://doi.org/10.3847/1538-4365/ab2194)
- Schwarz, G. J., Ness, J.-U., Osborne, J. P., et al. 2011, *ApJS*, 197, 31, doi: [10.1088/0067-0049/197/2/31](https://doi.org/10.1088/0067-0049/197/2/31)
- Seccull, T., Fraser, W. C., & Puzia, T. H. 2021, *PSJ*, 2, 57, doi: [10.3847/PSJ/abe4d9](https://doi.org/10.3847/PSJ/abe4d9)
- Seccull, T., Fraser, W. C., Puzia, T. H., Brown, M. E., & Schönebeck, F. 2018, *ApJL*, 855, L26, doi: [10.3847/2041-8213/aab3dc](https://doi.org/10.3847/2041-8213/aab3dc)
- Sheppard, S. S. 2010, *AJ*, 139, 1394, doi: [10.1088/0004-6256/139/4/1394](https://doi.org/10.1088/0004-6256/139/4/1394)
- . 2012, *AJ*, 144, 169, doi: [10.1088/0004-6256/144/6/169](https://doi.org/10.1088/0004-6256/144/6/169)
- Sheppard, S. S., & Trujillo, C. A. 2006, *Science*, 313, 511, doi: [10.1126/science.1127173](https://doi.org/10.1126/science.1127173)
- Wong, I., & Brown, M. E. 2017, *AJ*, 153, 145, doi: [10.3847/1538-3881/aa60c3](https://doi.org/10.3847/1538-3881/aa60c3)